Journal of Materials Chemistry A

PAPER

View Article Online
View Journal | View Issue

Check for updates

Cite this: J. Mater. Chem. A, 2017, 5, 21836

Elucidating the role of the hole-extracting electrode on the stability and efficiency of inverted $CsSnI_3/C_{60}$ perovskite photovoltaics†

K. P. Marshall,[a] M. Walker,[b] R. I. Walton[a] and R. A. Hatton*[a]

The correlation between the stability of thin films of black (B)-γ $CsSnI_3$ perovskite in ambient air and the choice of supporting substrate is examined for the substrates: (i) soda-lime glass; (ii) indium tin oxide (ITO) glass; (iii) copper iodide (solution processed)/ITO glass; (iv) poly(3,4-ethylenedioxythiophene):poly(styrenesulfonate) (PEDOT:PSS)/ITO glass; (v) and an optically thin (8 nm) gold film electrode. The performance of (ii)–(v) as the hole-extracting electrode in inverted photovoltaic (PV) devices with a simple bilayer architecture is compared for a test condition of 1 sun continuous solar illumination in air. $CsSnI_3$ film stability is shown to depend strongly on the density of pinholes and grain boundaries, although not on the preferred $CsSnI_3$ crystallite orientation. Solution processed CuI is shown to be unsuitable as a hole-transport layer (HTL) for inverted $CsSnI_3$ PV devices because it is almost completely displaced by the $CsSnI_3$ precursor solution during the spin coating process, and its large ionisation potential is poorly matched to the valence band edge of $CsSnI_3$. Devices using an ITO (or Au) hole-extracting electrode with no HTL are found to be more stable than those using the archetypal HTL; PEDOT:PSS. Spectroscopic analysis of the $CsSnI_3$ layer recovered from PV devices after 24 hours testing in ambient air (with no device encapsulation) shows that ≤11% of the $CsSnI_3$ film thickness is oxidised to Cs_2SnI_6 due to air ingress, which shows that the deterioration in device efficiency under continuous illumination does not primarily result from a reduction in the light absorption capability of the perovskite film due to $CsSnI_3$ oxidation. Additionally it is shown that $SnCl_2$ added during $CsSnI_3$ film preparation reduces the extent of p-type self-doping of the perovskite film and serves as an n-type dopant for the adjacent evaporated C_{60} electron transport layer.

Received 10th July 2017
Accepted 14th September 2017

DOI: 10.1039/c7ta05967a

rsc.li/materials-a

Open Access Article. Published on 06 October 2017. Downloaded on 3/29/2024 1:21:09 PM.
This article is licensed under a Creative Commons Attribution 3.0 Unported Licence.

Introduction

Lead halide perovskites have been intensively researched for use in photovoltaics (PVs) since 2009,[1] and have already achieved a certified power conversion efficiency (η) of 22.1%, which is approaching that of conventional silicon PVs.[2] However, the possibility of Pb contamination of the environment as a result of failure of the device encapsulants and/or improper disposal at the end of life is a serious concern for commercial exploitation because Pb is known to have high toxicity and can accumulate in the food chain.[3–6] This problem is particularly acute for Pb perovskites because they decompose in the presence of moisture to form water soluble toxic lead compounds such as PbI_2 and $PbCO_3$.[7,8] Consequently there is a need to identify perovskite semiconductors suitable for PVs that use lower toxicity replacements for Pb. Tin halide perovskites are one such possibility, and are also particularly attractive because of their lower band gaps than lead analogues (typically 1.3–1.4 eV), which are ideal for single junction PVs, very low exciton binding energies (<20 meV) and very large charge carrier mobilities (1–100 $cm^2\ V^{-1}\ s^{-1}$) which collectively bode very well for the possibility of achieving a η comparable to that of Pb perovskites.[9–12] However, Sn perovskites have not been widely researched because of the instability of Sn in the 2+ oxidation state, which is easily converted to the 4+ state in the presence of moisture and oxygen.[9,13] Additionally, Sn halide perovskites are susceptible to the formation of a high density of Sn vacancy defects which can severely limit the device fill factor (FF) and open-circuit voltage (V_{oc}).[12,14]

One approach to minimising tin vacancy density in Sn perovskites is to synthesise the perovskite in a Sn-rich environment,[12,14–16] although for device applications consideration must also be given to the fate of the compound supplying the excess Sn once the perovskite has formed, since the two components inevitably form a complex two-phase film.[12,17,18] We have recently shown that $SnCl_2$ is particularly effective as a source of excess Sn when synthesising $CsSnI_3$ perovskite, and is pushed to the surface of the $CsSnI_3$ crystallites where it serves the additional role of doping the adjacent phenyl-C_{61}-butyric acid methyl ester (PCBM) when the perovskite film is integrated

[a]Department of Chemistry, University of Warwick, Coventry, CV4 7AL, UK. E-mail: Ross.Hatton@warwick.ac.uk

[b]Department of Physics, University of Warwick, Coventry, CV4 7AL, UK

† Electronic supplementary information (ESI) available. See DOI: 10.1039/c7ta05967a

This journal is © The Royal Society of Chemistry 2017

Open Access Article. Published on 06 October 2017. Downloaded on 3/29/2024 1:21:09 PM.
This article is licensed under a Creative Commons Attribution 3.0 Unported Licence.

into an inverted device architecture.[17] Importantly $SnCl_2$ does not significantly increase the toxicity of the material system; indeed it is used an antioxidant in food, known as E512 in Europe.[19]

The stability of lead perovskite PVs is known to depend strongly dependent on the choice of materials used for the extraction of holes from the perovskite layer, particularly in inverted device architectures, where it not only ensures optimal interfacial energy level alignment for selective extraction of holes but is also a key determinant of perovskite film structure and morphology.[20–22] Herein we report the results of a study focused on how the stability of inverted $CsSnI_3$ PV devices with the structure: hole-extracting window electrode|$CsSnI_3$:$SnCl_2$-|C_{60}|bathocuproine (BCP)|Al depends on the choice of hole-extracting substrate. The hole-extracting electrode materials compared are: (i) ITO coated glass, because it is the most widely used transparent electrode and is sufficiently smooth to be used in simple bilayer perovskite PV device architecture without an additional layer to smooth the electrode surface. This system serves as the benchmark against which the others are compared; (ii) ITO/copper iodide (CuI), because CuI has recently been used for both Pb[23–25] and Sn[15] based PPVs, and is reported to be a very stable hole-transport layer (HTL) for Pb perovskite PV applications;[23–25] (iii) ITO/poly(3,4-ethylenedioxythiophene):poly(styrenesulfonate) (PEDOT:PSS), because it is the most widely used HTL used in inverted Pb perovskite PV research[26–28] and, due to the very high doping level PEDOT:PSS can be regarded as a synthetic metal; (iv) an optically thin (8 nm thick) Au electrode supported on glass fabricated using the molecular adhesive layer method,[29] because Au is widely used in perovskite PV research due to its high stability and, in the context of this study, serves as a chemically stable and structurally well-defined[29,30] model electrode. To date the stability of Sn PVs towards complex conditions (*i.e.* constant 1 sun illumination, moisture, elevated temperature) have been sparsely reported,[18,31–33] and to our knowledge this is the first report comparing the stability of inverted Sn perovskite PV with the choice of hole-extracting electrode/HTL.

Experimental

B-γ $CsSnI_3$ film deposition

In a dry nitrogen filled glove box (<1 ppm H_2O and O_2), SnI_2, CsI and $SnCl_2$ were added to a vial in a 1 : 1 : 0.1 ratio. Anhydrous *N*,*N*-dimethylformamide (DMF) was added to make the solution up to 8 wt% by total mass of solids, and left overnight to allow the material to dissolve. One drop of solution was cast onto a substrate spinning at 4000 rpm, and allowed to spin for 60 seconds to form $CsSnI_3$:$SnCl_2$ films with an intense dark red/brown colour. The films formed while spinning as the solvent evaporates.

Photovoltaic device fabrication

ITO coated glass slides were cleaned by immersing in acetone and placing in an ultrasonic bath for 10 minutes. This process was repeated using high purity water containing a few drops of Decon 90 surfactant, then with water only and finally isopropanol. The slides were then suspended in boiling acetone vapour for 10 seconds and dried in a flow of nitrogen, before UV/O_3 treatment for 15 minutes using a 185/254 nm light source, before being transferred into the glovebox for device fabrication.

CuI was spin cast from 50 mg ml^{-1} di-*n*-propylsulfide solutions at 2000 rpm, and left in the glovebox for 30 minutes to dry. $CsSnI_3$ was spin cast at 4000 rpm from 8 wt% DMF solution.

C_{60} was deposited by thermal evaporation at ~500 °C at a rate of 0.5 to 1 Å s^{-1} to a thickness of 40 nm. Bathocuproine (BCP) was thermally evaporated at ~140 °C at a rate of ~0.5 Å s^{-1} to a thickness of 6 nm. Al was evaporated at a rate of 1 Å s^{-1} to a thickness of 50 nm.

8 nm Au electrode fabrication

Au films with a thickness of 8 nm were fabricated on glass substrates using the procedure previously reported by our group.[29] In brief, glass microscope slides were cleaned and exposed to vapour of 3-aminopropyltrimethoxysilane and 3-mercaptopropyltrimethoxysilane in a desiccator at 40 mbar. The Au films were UV/O_3 treated for 15 minutes immediately prior to $CsSnI_3$ deposition.

X-ray diffraction (XRD)

XRD was performed on thin films of $CsSnI_3$ prepared from 8 wt% (total solids) DMF solution deposited onto a substrate spinning at 4000 rpm for 60 s. Scans were recorded under a flow of nitrogen using a Cu $K\alpha_{1/2}$ source in θ–θ mode on a Bruker D8 Advance powder diffractometer equipped with an Anton-Paar HTK900 gas chamber. The measured XRD patterns were corrected for height offset (due to the height of the glass substrate) by calibrating the 2θ scale with reference to the expected peak positions for pure B-γ $CsSnI_3$. Simulated diffraction patterns were calculated using the program, Mercury 3.5.1 (ref. 35) using crystallographic information files from the Inorganic Crystal Structure Database (ICSD).

Photoelectron spectroscopy

X-ray photoelectron spectroscopy (XPS) and ultra-violet photoelectron spectroscopy (UPS) were performed on samples supported on Au coated glass using a Kratos AXIS Ultra DLD at a base pressure of 5×10^{-11} mbar. Samples were loaded into the spectrometer using an air tight sample transfer arm that enables transfer from the glovebox to the spectrometer without exposure to air. Au electrodes were UV/O_3 treated for 15 minutes before sample deposition to achieve compact perovskite films. For XPS analysis the sample was excited with X-rays from a monochromated Al Kα source ($h\nu$ = 1486.7 eV), with the photoelectrons being detected at a 90° take-off angle. Peak fitting was performed using the CasaXPS package,[36] incorporating Voigt (mixed Gaussian–Lorentzian) line shapes and a Shirley background. UPS was performed in the same vacuum system as for XPS using a 21.22 eV He 1α light source.

Open Access Article. Published on 06 October 2017. Downloaded on 3/29/2024 1:21:09 PM.
This article is licensed under a Creative Commons Attribution 3.0 Unported Licence.

Electronic absorption spectroscopy

Ultraviolet/visible/near-infrared spectra were measured for optically thin films of $CsSnI_3$ on glass or ITO glass substrates.

Optical field and electronic absorption simulations

The Essential Macleod V 9.7 (ref. 34) software simulation package was used for simulating light intensity in devices.

Contact potential measurement

Work function measurements were performed using a Kelvin probe referenced to freshly cleaved highly oriented pyrolytic graphite in a nitrogen-filled glovebox co-located with the spin coater and thermal evaporator.

Atomic force microscopy (AFM)

AFM was performed on a Veeco Multimode using films on glass substrates. Analysis was performed using the program WSxM 4.0.[37]

Scanning electron microscopy (SEM)

SEM imaging was performed using a Zeiss SUPRA 55VP field emission gun SEM and crystallite size analysis was performed using the ImageJ[38] program.

Results & discussion

B-γ $CsSnI_3$ film structure and stability on different substrates

The perovskite B-γ $CsSnI_3$ is known to degrade in ambient air in a two-stage process; firstly into the one dimensional yellow phase of $CsSnI_3$ (Y-$CsSnI_3$) with the same chemical composition upon reaction with moisture and then into the zero-dimensional Sn(IV) salt Cs_2SnI_6 upon reaction with oxygen[9,13,17] the latter of which has an absorption coefficient across the visible spectrum ~10× smaller than that of B-γ $CsSnI_3$.[11] Exploiting the large reduction in absorption strength upon oxidation to Cs_2SnI_6, the evolution of the absorption spectrum of thin films of $CsSnI_3$ supported on the different substrates was used to follow the oxidation of $CsSnI_3$ films in air: Fig. 1(a)–(c).

It is evident from Fig. 1 that the stability of $CsSnI_3$:$SnCl_2$ films decreases in the order ITO glass > glass ≈ CuI/ITO glass > PEDOT:PSS/ITO glass > Au. Whilst glass is not useful as an electrode it is a simple transparent reference substrate against which the optical properties of the perovskite film on the other more complex substrates can be compared. The spectrum of $CsSnI_3$:$SnCl_2$ on ITO includes a broad local minimum at ~400 nm that is not a feature of $CsSnI_3$ films on all of the other substrates; Fig. 1(a) and (b) and ESI Fig. S1(a)–(c),† although optical modelling reveals that this feature results from an optical interference effect (Fig. S2†) rather than from a difference in electronic structure.

The stability of $CsSnI_3$:$SnCl_2$ films supported on different HTL/electrodes towards air-oxidation is inevitably a complex function of: (i) the intrinsic stability of the perovskite film (which strongly dependents on its morphology, including the crystallite size and orientation); (ii) the density of pinholes and

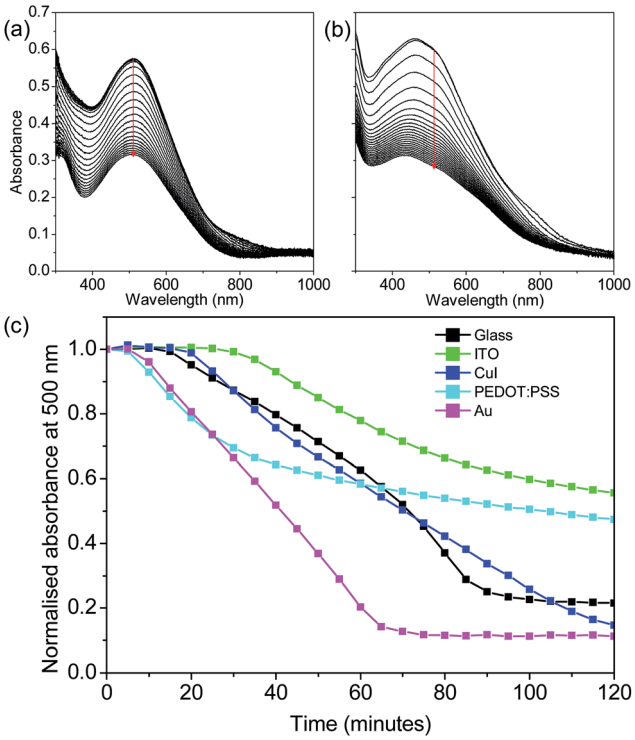


Fig. 1 Evolution of electronic absorption spectrum of $CsSnI_3$ + 10 mol% $SnCl_2$ films deposited on ITO glass (a) and PEDOT:PSS (b) when exposed to ambient air (RH = 38%). Fig. 1(c) shows the evolution of absorbance at a wavelength of 500 nm for $CsSnI_3$:$SnCl_2$ films on ITO, ITO:CuI, ITO:PEDOT:PSS, Au and glass. In all cases the $CsSnI_3$ solution concentration was 8 wt% which resulted in a film thickness of ~50 nm. In each case the background has been subtracted.

fissures in the film which determines the surface area of film exposed to the environment, and therefore its susceptibility to oxidation; (iii) the intrinsic stability of the underlying substrate material(s) towards oxidation in air; (iv) and the intrinsic stability of the interfaces between the films, and the relative importance (i)–(iv) is not easily disentangled. It is however evident from Fig. 1 and 2 that for perovskite films on ITO glass, glass, CuI and PEDOT:PSS the decrease in perovskite film stability correlates with a decrease in the perovskite coverage of the underlying substrate: excluding the perovskite film on Au, the film on ITO glass is the most compact with a significant number density of pin-holes with diameter 15–25 nm. On CuI the perovskite film has a high density of elongated fissures along grain boundaries, while on the PEDOT:PSS substrate the perovskite film is non-uniform with some regions being densely packed with a pinhole density and pin-hole size comparable to that on ITO glass (Fig. 2(e)), and others have a high density of large fissures (Fig. 2(d)). The decrease in stability with reduced perovskite coverage of the underlying substrate can be rationalised in terms of the greater surface area of the perovskite film presented to the oxidising environment. The stability of the underlying substrate towards ambient air may also play a role given that PEDOT:PSS is known to be hygroscopic[39] and the first stage of $CsSnI_3$ film oxidation (*i.e.* conversion of B-γ $CsSnI_3$ to Y-$CsSnI_3$) results from the interaction with water.[17] The stability

This journal is © The Royal Society of Chemistry 2017

Open Access Article. Published on 06 October 2017. Downloaded on 3/29/2024 1:21:09 PM.
This article is licensed under a Creative Commons Attribution 3.0 Unported Licence.

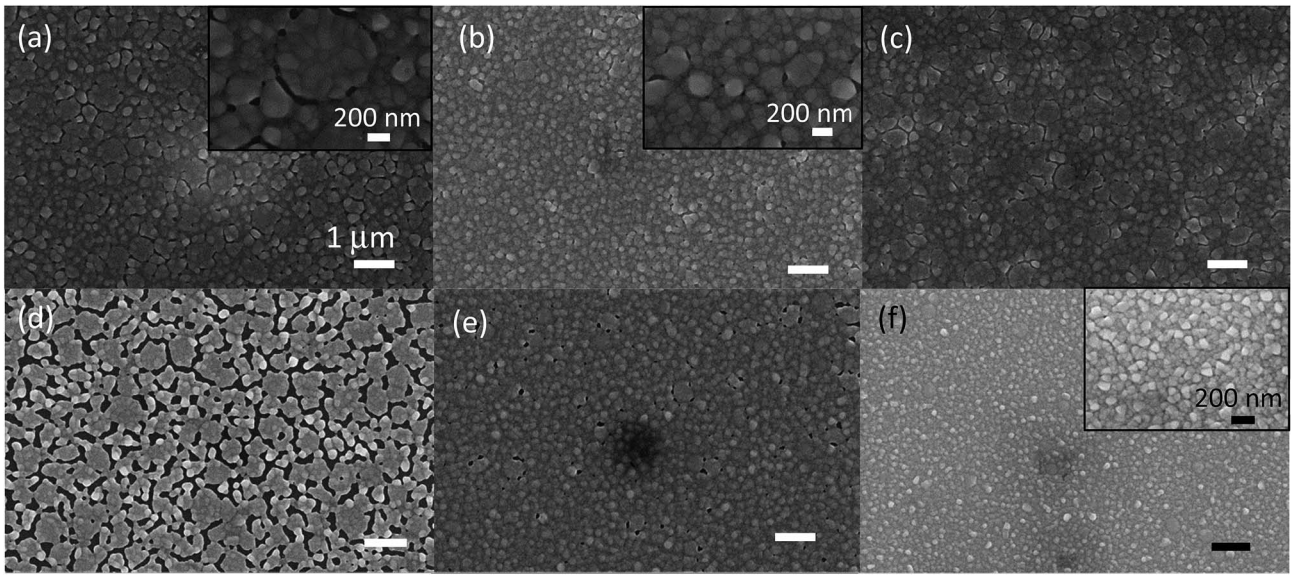


Fig. 2 SEM images of $CsSnI_3$ + 10 mol% $SnCl_2$ deposited on top of (a) glass, (b) ITO, (c) CuI, (d) PEDOT:PSS (low coverage section), (e) PEDOT:PSS (high coverage area), (f) Au. The scale bar (b)–(f) is equal to 1 μm.

of $CsSnI_3$:$SnCl_2$ film on Au does not follow this trend because it is the least stable towards air-oxidation whilst also has the most compact and uniform film morphology with a relatively low density of very small (13–17 nm) pinholes. Given that the Au electrode is stable in ambient air,[29] the poor stability of the $CsSnI_3$:$SnCl_2$ film on Au most likely stems from instability in the perovskite film itself. Close inspection of the SEM images in Fig. 2(b) and (f) reveals that $CsSnI_3$:$SnCl_2$ films on Au have the smallest and most uniform crystallite sizes; ~2200 nm^2 *vs.* ~4900 nm^2 on ITO glass, and so it is likely that the higher density of grain boundaries enables more rapid water and oxygen penetration into the film, giving rise to increased instability despite the high film coverage of the underlying substrate, as previously been reported for lead halide perovskites.[40] Collectively these observations show that the stability of $CsSnI_3$ films towards air oxidation depends not only on the density of microscopic pin-holes and fissures but also on the density of grain boundaries between $CsSnI_3$ crystallites, with highest stability offered by perovskite films that are compact and comprise larger crystallites.

X-ray diffraction (XRD) was used to confirm that the B-γ phase of $CsSnI_3$ is formed, and to investigate the possibility that the stability of the perovskite films depends on the orientation of the crystallites making up the film, since different crystal faces would be expected to have different reactivity towards water and oxygen, due to the different arrangement and density of atoms presented to the atmosphere (Fig. 3).

The XRD patterns shown in Fig. 3 confirm the presence of only B-γ $CsSnI_3$ on all substrates, and indicate that there is a preferred orientation for crystallites on CuI and Au, because the intensity of the reflection at ~29° (202 and 040) is greatly increased as compared to that at ~25° (220 and 022). However, the large differences in preferred crystallite orientation do not correlate with film stability towards oxidation in air, since films on CuI and Au have very similar preferred orientation, but very different stability in air (Fig. 1(c)).

Solution processed CuI has been reported to be an effective as a HTL in lead perovskite PV prepared using DMF as the solvent for perovskite deposition.[23,24] However, whilst the SEM image in Fig. 2(c) shows that $CsSnI_3$ films on CuI have high coverage of the underlying substrate, the XRD pattern; Fig. S4,† shows complete disappearance of the intense CuI (111) peak when a $CsSnI_3$ film is deposited on top of a CuI film by spin coating, indicating the ~40 nm CuI film is dissolved and displaced by the $CsSnI_3$ solution during the spin coating process. This conclusion is supported by the absorption spectrum of the perovskite film deposited on CuI; Fig. S5,† which shows only a small perturbation of shape of the $CsSnI_3$:$SnCl_2$ spectrum at wavelengths below ~350 nm, which corresponds to the onset of strong absorption in CuI. Additionally, cross-sectional AFM image analysis of scored CuI/$CsSnI_3$:$SnCl_2$ films; Fig. S6,† shows

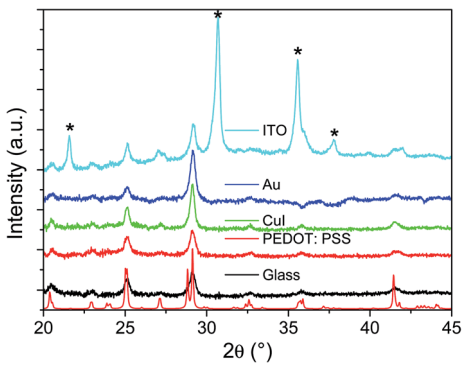


Fig. 3 XRD patterns of films of $CsSnI_3$ + 10 mol% $SnCl_2$ on ITO, Au, CuI, PEDOT:PSS and glass substrates and simulated. Also shown is the simulated B-γ $CsSnI_3$ spectrum (bottom). Asterisks (*) indicate reflections associated with the ITO background (Fig. S3†).

Open Access Article. Published on 06 October 2017. Downloaded on 3/29/2024 1:21:09 PM.
This article is licensed under a Creative Commons Attribution 3.0 Unported Licence.

that the measured thickness of the film is 35–40 nm, which is only half the combined thickness of separate CuI and perovskite overlayer. Energy-dispersive X-ray analysis of the films (Fig. S7 and Table S1†) also show that Cu is barely detectable in CuI/$CsSnI_3$:$SnCl_2$ films supported on ITO glass, whilst the indium signal from the underlying ITO substrate is very intense. AFM imaging and electronic absorption spectroscopy of CuI films before and after spin casting DMF, Fig. S8(a–c),† reveal that CuI films are partially soluble in DMF, which would be expected to give rise to a complex interpenetrating interface between the CuI and perovskite overlayer, with a significant amount of CuI remaining at the interface between the ITO glass and the perovskite film. However, the weight of experimental evidence is consistent with almost complete displacement of the ~40 nm CuI film to form a perovskite film with comparable crystallinity and film coverage to that achieved on ITO glass without Cu, which is unexpected given the very rapid speed of the perovskite film formation during spin coating process. It is known that CuI is soluble in concentrated aqueous solutions of iodide ion,[41] and so it is plausible that in this case the iodide concentration in the DMF solution used to prepare the perovskite films is sufficiently high to make the solution a very powerful solvent for CuI, which together with the tendency of $CsSnI_3$ to crystallize very rapidly from DMF[42] results in the near complete displacement of the CuI film, rendering CuI unsuitable a HTL in inverted $CsSnI_3$ PV devices.

Photovoltaic device studies

Stability studies under 1 sun continuous illumination in ambient air without device encapsulation were performed on PV devices identical in every respect, except in the choice of hole-extracting electrode and/or HTL, as schematically illustrated in Fig. 4(a).

Ingress of ambient air into a PV device is inevitable even with encapsulation (given sufficient time) and so testing in air under constant illumination is a test condition of practical relevance. However, the degradation mechanisms under such complex conditions are inevitably multi-faceted, with a number of parallel mechanisms operating over different time scales.[43] For this reason the device structure used to investigate the correlation between device stability and the choice of hole-extracting substrate is based on a simple discrete layer architecture.

It is evident from Fig. 3 and 5 that there is no strong correlation between the preferred crystallite orientation and device stability towards oxidation, since the rate of reduction in absolute efficiency of devices using Au and ITO electrodes is similar, even though a preferred crystallite orientation is much more evident for $CsSnI_3$ films on Au. Consequently, whilst crystallite orientation may play some role in determining $CsSnI_3$ film stability towards air-oxidation, it is much less important than the role of pinholes and grain boundaries between crystallites. For the champion device using ITO only the hole-extracting electrode the efficiency degrades to 70% of its initial value only after ~20 hours which is comparable to the highest reported for unencapsulated Sn perovskite based PV devices tested under constant illumination in ambient air.[17,18,31–33,44]

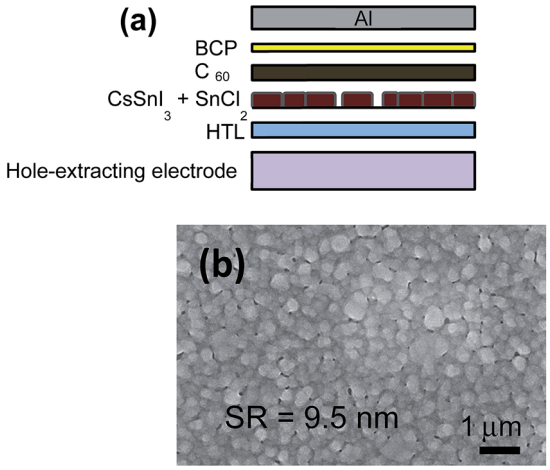


Fig. 4 (a) Schematic diagram of the model device architecture used in this study, including $CsSnI_3$ with pinholes. (b) SEM image of the surface morphology C_{60} deposited by vacuum evaporation onto a ~50 nm thick $CsSnI_3$ film supported on ITO glass. The root-mean-square surface roughness (SR) (measured using atomic force microscopy) is given on the image.

The primary reason for the deterioration in the power conversion efficiency of devices using ITO (only) and Au as the hole extracting electrode over the first 24 hours testing in air is the ~50% loss in short circuit current density (J_{sc}), which almost certainly results from several parallel processes some of which will be unrelated to the perovskite layer. For example, it is known that exposure of C_{60} to ambient air deteriorates its conductivity due to doping by H_2O and O_2, which trap electrons.[45,46] BCP is also known to crystallise when exposed to air (a process that will be accelerated by the elevated temperature under the solar simulator; ~50 °C) forming electron trap states at the interface between crystallites.[47] Air ingress into the device through pin holes in the Al electrode is also known to result in the formation of an insulating Al_2O_3 layer at the in BCP/Al interface.[48–50] Any of these processes could give rise to the observed increase in device series resistance, which is evident from the decrease in gradient of the *J–V* characteristic where it crosses the voltage axis: Fig. S9(a)–(c).†

Assuming the efficiency of hole-extraction across the buried interface between the ITO (or Au) electrode and perovskite remains unchanged, any reduction in the efficiency of electron extraction to the external circuit as a result of any of the aforementioned degradation processes would be expected to increase recombination losses in the perovskite layer, offering a plausible explanation for the observed decline in J_{sc}.[51] However, air ingress into the device would also be expected result in oxidation of the $CsSnI_3$ to form Cs_2SnI_6,[17] resulting in two additional mechanisms for J_{sc} degradation: (i) Cs_2SnI_6 is a semiconductor with an absorption coefficient across the visible spectrum ~10× smaller than that of B-γ $CsSnI_3$, and so the transformation of $CsSnI_3$ into Cs_2SnI_6 would reduce the light harvesting capability of the device, thereby reducing J_{sc}; (ii) the work function and energy of the valence band edge of Cs_2SnI_6 (prepared by air oxidation of $CsSnI_3$) measured using ultra-violet photo-electron spectroscopy (UPS) as part of this

 This journal is © The Royal Society of Chemistry 2017

Open Access Article. Published on 06 October 2017. Downloaded on 3/29/2024 1:21:09 PM.
This article is licensed under a Creative Commons Attribution 3.0 Unported Licence.

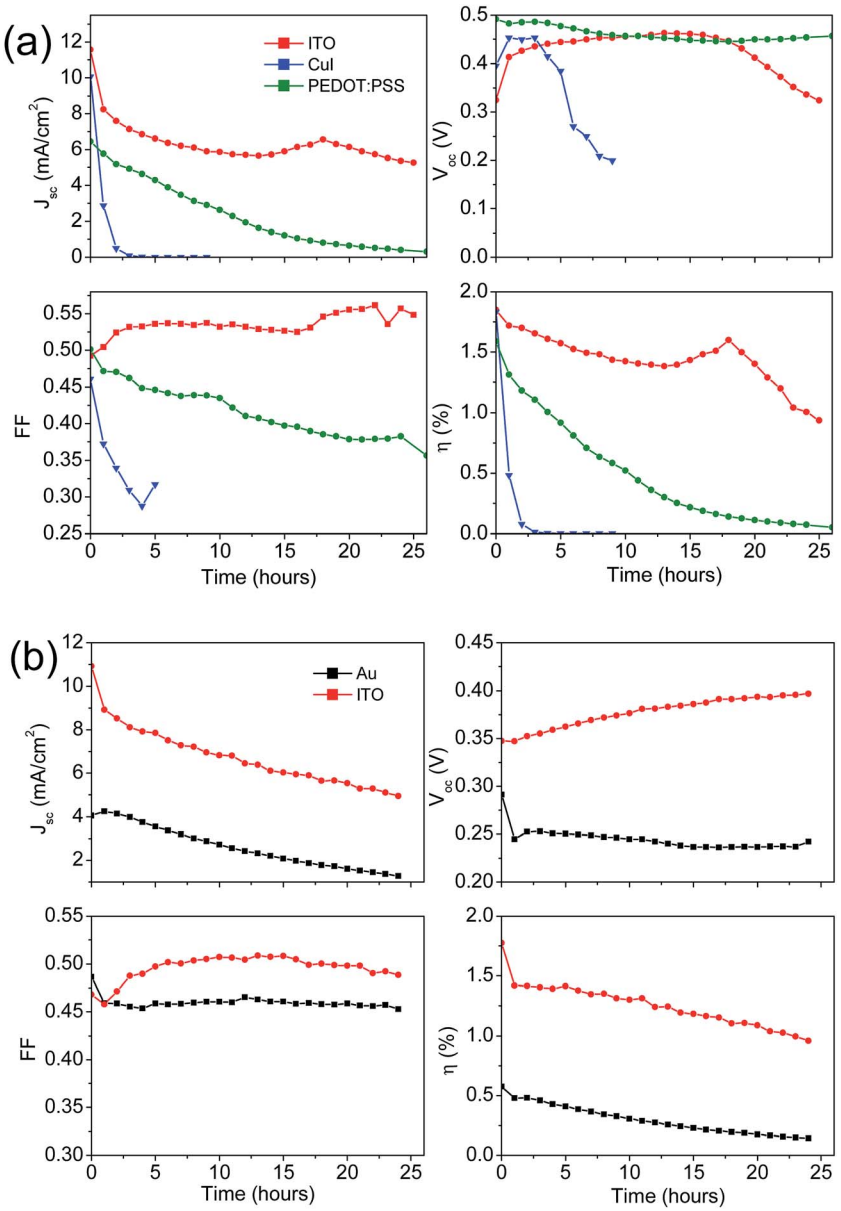


Fig. 5 Representative performance of 6 mm^2 $CsSnI_3$:$SnCl_2$ PPV devices with the structure shown in Fig. 4(a) and without device encapsulation, tested in ambient air (humidity of ~25%) under constant 1 sun simulated solar illumination. After 45 minutes the device temperature had stabilised at ~50 °C. The devices tested were identical in every respect except for the choice of hole-extracting electrode/HTL: ITO (a & b), PEDOT:PSS (a), CuI (a), or Au (b) substrates. The performance of devices using ITO only, tested in a nitrogen atmosphere (<1 ppm O_2, <1 ppm H_2O) is given in the ESI Fig. 10.†

study with special care to remove adsorbed water and carbon contaminants; Fig. S11,† are 5.1 eV and 5.83 eV below the vacuum level, respectively. Given that the band gap of Cs_2SnI_6 has been reported to be ~1.3 eV (ref. 11 and [52]) and ~1.6 eV,[53] the conduction band edge in Cs_2SnI_6 is estimated to be in the range 4.2–4.5 eV below the vacuum level (Fig. 6). Whilst both of these limits are well below the energy of the conduction band edge in $CsSnI_3$; 3.6 eV,[17] and the lowest unoccupied molecular orbital energy of C_{60}; 4.0 eV,[54] at the real interface between $CsSnI_3$ and Cs_2SnI_6 electron transfer from the $CsSnI_3$ into Cs_2SnI_6 would be expected to occur, driven by the differences in Fermi level energy, which would reduce the barrier to electron transport across this interface possibly to <0.1 eV. There is also a large degree of uncertainty as to the extent of charge transfer at the Cs_2SnI_6/C_{60} interface, which will depend on the local $SnCl_2$ doping level in the C_{60} layer. Consequently it is not possible to know with a high degree of accuracy the extent to which the formation of Cs_2SnI_3 at the interface between $CsSnI_3$ and C_{60} would impede the flow of electrons to the external circuit, giving rise to an increase in device series resistance. However, it can be concluded that Cs_2SnI_6 formed at the $CsSnI_3/C_{60}$ interface due to air ingress into the device would serve as reservoir of trapped electrons occupying energy states with energies in the band gap of the $CsSnI_3$, the presence of which

Open Access Article. Published on 06 October 2017. Downloaded on 3/29/2024 1:21:09 PM.
This article is licensed under a Creative Commons Attribution 3.0 Unported Licence.

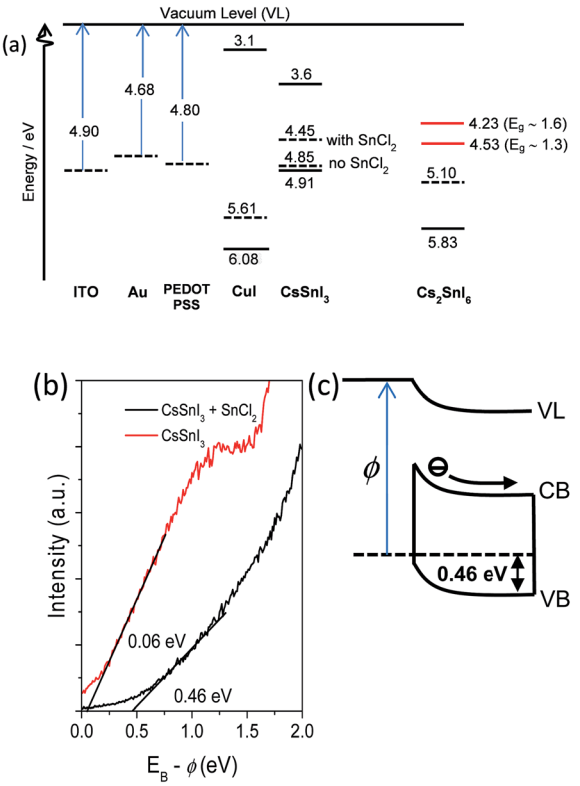


Fig. 6 (a) Schematic energy level diagram summarizing the energy of the valence band (VB) edge with respect to the vacuum level (VL), the work function (ϕ) and Fermi level (E_f) (dotted line) for each material used in this study. (b) UPS spectrum of $CsSnI_3$ and $CsSnI_3$:$SnCl_2$ at VB band edge. The small signal above E_f (*i.e.* $E_B - \phi > 0$ eV) results from ~1% of the incident UV photons from the UV lamp having energy >21.22 eV. (c) Energy level diagram depicting the Schottky contact between the $CsSnI_3$:$SnCl_2$ and the ITO electrode.

would be expected to erode J_{sc} due to increased recombination loses.

To determine the extent of formation of Cs_2SnI_6 in an actual devices, devices with a cell area of ~74 mm^2 were fabricated and tested under continuous 1 sun simulated illumination for 24 hours: Fig. S12.† The evolution of V_{oc}, FF and J_{sc} of these larger cell area devices is very similar to that for much smaller area (6 mm^2) devices shown in Fig. 5, and is discussed in detail in the next part of this paper. Following device stability testing the C_{60}, BCP and Al layers were removed by peeling off the Al electrode followed by repeated washing with chlorobenzene, and the absorption spectrum of the remaining $CsSnI_3$ measured to determine the extent of film oxidation: Fig. S13(a).† Most strikingly, the rate of degradation of light absorption by the perovskite film after 24 hours testing is much slower than the rate of degradation in J_{sc}: after 24 hours J_{sc} has decreased by ~75% (~50% in 6 mm^2 devices) whilst the absorption intensity (@500 nm) is reduced only by 0–11% over the same time period (Fig. S12†). Quantification of the reduction in absorption intensity with a higher degree of certainty is not possible because the variation in absorbance for $CsSnI_3$ films prepared in the same way is comparable to the reduction in absorbance intensity for films in devices after 24 hours testing; Fig. S13(b).†

High resolution XPS analysis of the perovskite film following removal of the C_{60}, BCP and Al layers after 24 hours continuous illumination testing gives the thickness of the Cs_2SnI_6 layer to be ~3% (or ~1.5 nm): Fig. S14.† Whilst there is uncertainty associated with this value, due to the presence of a small but significant Cl 2p peak in the XPS spectrum (Fig. S14 lower†) which indicates the presence of residual $SnCl_2$, it is well within the range determined from the electron absorption spectroscopy. This finding indicates that the large deterioration in J_{sc} – which is the primary reason for the degradation in device efficiency – does not primarily result from a reduction in the light absorption capability of the perovskite film due to oxidation of the $CsSnI_3$ layer. Indeed, for a tin perovskite PV, such a low level of perovskite oxidation after 24 hours continuous illumination in air without encapsulation is remarkable.

The most striking conclusion from a comparison of the device performance (Fig. 5) is that devices with an ITO or Au electrode without a HTL have superior stability to those using the archetypal HTL layer PEDOT:PSS. The high stability of devices using the Au electrode is also counter to that expected on the basis that the $CsSnI_3$ film stability measurements (Fig. 1). To rationalise the latter, it is necessary to take into account not only the intrinsic stability of each semiconductor layer making up the device but also their combined morphology, since the morphology and uniformity of the Al top electrode is strongly dependant on that of the underlying materials. Since the Al electrode is the primary barrier to the ingress of water and oxygen in these devices,[50,55] any fine gaps or pinholes in the Al electrode resulting from the high surface roughness of the semiconductor layers onto which it is deposited will have a major adverse effect on device stability.[56,57] In this work all of the organic semiconductor layers are thermally evaporated to guarantee a high degree of control and reproducibility film thickness. However, unlike solution processed organic semiconductors, evaporated organic semiconductor layers tend to have a morphology very similar to that of the substrate onto which they are deposited, and so the pinholes in the $CsSnI_3$:$SnCl_2$ film are also present in the C_{60} over layer (Fig. S15†). Consequently, organic semiconductor films vacuum deposited onto a very uniform and compact perovskite film, such as that formed on Au (Fig. 2(f)), can be expected to have a reduced number of defects in the C_{60}, BCP and Al layers that may allow H_2O and O_2 ingress into the device.

The simplest explanation for the inferior device stability using PEDOT:PSS/ITO glass electrode is that the low surface coverage in many areas (Fig. 2(d)) and its well-known hygroscopic properties.[58] The latter is particularly problematic for $CsSnI_3$ because it is known to degrade in the presence of water to form Y-$CsSnI_3$, or Cs_2SnI_6 when oxygen is also present.[9,13] However, it is also notable that the rate of degradation in efficiency is much more pronounced than on ITO because the FF and V_{oc} do not initially improve, as is observed to be the case for devices using ITO without a PEDOT:PSS layer. The initial improvement in these parameters for devices using ITO without a HTL occurs over several hours under constant illumination and is similar to that previously reported to occur after a period of extended storage in a nitrogen filled glovebox for devices

 This journal is © The Royal Society of Chemistry 2017

Open Access Article. Published on 06 October 2017. Downloaded on 3/29/2024 1:21:09 PM.
This article is licensed under a Creative Commons Attribution 3.0 Unported Licence.

using $PC_{61}BM$ in place of evaporated C_{60}.[17] The latter was shown to result from n-type doping of the $PC_{61}BM$ by the $SnCl_2$, which results in the formation of a Schottky barrier to parasitic electron extraction by the ITO electrode at the site of small pinholes in the perovskite film.[17] Direct evidence for an n-type doping interaction between evaporated C_{60} and $SnCl_2$ is provided by high resolution X-ray photo-electron spectroscopy (Fig. S16 and S17†), which shows that the binding energies of the Cl 2p electrons in $SnCl_2$ incorporated into a C_{60} film are 198.8–199.1 eV ($2p_{3/2}$) and 200.5–200.8 eV ($2p_{1/2}$), which are ~0.6 eV higher than that of $SnCl_2$; 198.2 eV and 199.8 eV respectively.[17] This large chemical shift to higher binding energy is consistent with partial electron transfer from the $SnCl_2$ into the C_{60}, similar to that reported to occur between $SnCl_2$ and PCBM.[17] It is reasonable to expect that diffusion of $SnCl_2$ into C_{60} is accelerated by the heating under the solar simulator lamp, since after 45 minutes exposure to one sun simulated solar illumination the devices stabilise at a temperature of ~50 °C, and so C_{60} at the site of pin-holes in the $CsSnI_3$ film takes time to become optimally doped with $SnCl_2$.

The dark current–voltage characteristics of the same devices before and after five hours continuous illumination plotted on a log-linear scale (Fig. S18†) validate the conclusion that a barrier to parasitic electron extraction forms at the ITO electrode, since the dark current in reverse bias is dramatically reduced. Within the framework of this model the lack of improvement in V_{oc} and FF for devices using PEDOT:PSS can be understood in terms of the very large size of the holes in $CsSnI_3$:$SnCl_2$ layer on PEDOT:PSS (Fig. 1(d)), because the $SnCl_2$ concentration in the C_{60} at the site of these large holes is unlikely to be as high as at the site of the much smaller pinholes in the $CsSnI_3$:$SnCl_2$ layer on ITO (Fig. 1(b)) where $SnCl_2$ on the side walls of the $CsSnI_3$ crystallites will also be a significant source of $SnCl_2$. Conversely, the absence of any improvement in V_{oc} and FF for devices using an Au hole-extracting electrode can be explained by the very compact, almost pin-hole free morphology of the perovskite film on Au (Fig. 2(f)), which means that the aforementioned mechanism of improvement in FF and V_{oc} would not be operative.

CuI has been proposed as an attractive alternative to PEDOT:PSS for lead perovskite PV devices due to its wide band gap, and ease with which it can be solution processed to form thin films and high stability.[23–25] However, it is evidence from Fig. 6 that devices using CuI as the HTL are in fact very unstable, exhibiting a rapid deterioration in FF and J_{sc} when tested under continuous illumination. This instability is attributed to the previously discussed disordered nature and very low thickness of the CuI layer at the ITO/perovskite interface after perovskite deposition. Measurement of the work function and energy of the valence band edge with respect the vacuum level (Fig. S19 & 20†), schematically shown in Fig. 6, reveals that whilst the valence band in $CsSnI_3$ should be closely aligned with the valence band in CuI once thermodynamic equilibrium is established, holes could become trapped in the potential well at the interface between them, which would be expected to reduce J_{sc} by reducing the built-in electric field. However, the J_{sc} is in fact comparable to that using ITO with no HTL, which is consistent with the finding that the CuI layer is almost completely displaced by the perovskite film during $CsSnI_3$ film deposition.

Analysis of the valence band edge region in the UPS spectrum (Fig. 5(b)) shows that the difference in energy between the Fermi level (E_f) and the valence band in $CsSnI_3$ is increased by ~0.4 eV when $CsSnI_3$ is synthesised in the presence of 10 mol% $SnCl_2$. This large shift away from the valence band confirms that $SnCl_2$ serves to reduce the density of Sn vacancy defects, which are known to be the primary source of background carrier density in $CsSnI_3$.[14] It can be surmised from Fig. 6 that there should be no barrier to the extraction of photo-generated holes using ITO, Au or ITO| PEDOT:PSS since the work function (ϕ) of $CsSnI_3$:$SnCl_2$ is smaller than all of the hole-extraction electrodes/HTL materials investigated, and the valence band edge in $CsSnI_3$:$SnCl_2$ is lower in energy than the Fermi level in ITO, Au or PEDOT:PSS/ITO. Consequently, the energetics upon contact formation should facilitate hole-extraction, as schematically illustrated in Fig. 6(c). Notably, however, devices using ITO|PEDOT:PSS initially exhibit approximately half the J_{sc} of those using ITO only. Optical modelling of the optical field distribution in the PEDOT:PSS shows that this large difference in J_{sc} cannot be attribute to a difference in light intensity in the $CsSnI_3$ layer, which is comparable for devices with and without PEDOT:PSS (Fig. S21(a) and (b)†). The difference in J_{sc} can however be explained in terms of the difference in the ϕ of the PEDOT:PSS and ITO glass, because the former is ~0.1 eV smaller than that of ITO. Whilst the absolute magnitude of this difference it relatively small, it is significant compared to the difference in energy between the E_f in $CsSnI_3$:$SnCl_2$ and the hole-extracting electrode E_f (0.35–0.45 eV), which would result in a narrower depletion region in the $CsSnI_3$ when using PEDOT:PSS as the electrode. It is over the depletion region that photo-generated electrons and holes are most efficiently separated in a perovskite PV device,[59] and so reducing the width of the depletion region would be expected to reduce J_{sc} – as is observed to be the case. This rationale also offers a plausible explanation for the low J_{sc} in devices using an optically thin Au electrode, which have a J_{sc} only one third of that achieved using an ITO electrode, even though the far-field transparency of the Au electrode is approximately two thirds that of ITO glass.[29] Again, optical modelling confirms that the low J_{sc} cannot be explained in terms of the lower transparency of the Au electrode alone: Fig. S21(a) and (c).† However, the ϕ of the Au electrode is significantly smaller than that of ITO or PEDOT:PSS electrode, which would further reduce the depletion width, and thus the perovskite thickness over which photo-generated charge carriers are efficiency separated.

Conclusions

The key findings of this study are:

(1) Using five different types of substrate we have shown that the stability of thin films of B-γ $CsSnI_3$ perovskite towards oxidation in air depends strongly not only on the density of microscopic pinholes and fissures, but also on the density of grain boundaries between $CsSnI_3$ crystallites, with best stability

Open Access Article. Published on 06 October 2017. Downloaded on 3/29/2024 1:21:09 PM.
This article is licensed under a Creative Commons Attribution 3.0 Unported Licence.

offered by films that are compact and comprise of larger crystallites. X-ray diffraction measurements performed on perovskite films prepared in the same way as for PV devices, show that the stability of $CsSnI_3$ films towards oxidation in air is not strongly dependent on preferred orientation of the $CsSnI_3$ crystallites.

(2) We have shown that CuI is unsuitable as the HTL in $CsSnI_3$ inverted PV when using DMF as the solvent, because it is almost completely displaced by the $CsSnI_3$ precursor solution during the spin coating process and its large ionisation potential is poorly matched to the valence band edge of $CsSnI_3$. It is likely that a similar problem will arise if DMF is substituted with an alternative polar solvent.

(3) It is shown that unencapsulated PV devices based on an inverted bilayer device architecture using ITO or semi-transparent Au, as the hole-extracting electrode without a HTL are more stable than those using the archetypal hole-extraction material PEDOT:PSS when tested under 1 sun constant simulated illumination in ambient air. This difference is attributed to the inferior film forming properties of $CsSnI_3$ on PEDOT:PSS combined with its well-known hygroscopic nature. Whilst chemical modification of PEDOT:PSS to rectify the problem of film uniformity may be possible, the hygroscopic nature is a particular problem for $CsSnI_3$ based PVs because H_2O in known to initiate oxidation of $CsSnI_3$, and so hygroscopic materials immediately adjacent to $CsSnI_3$ should be avoided.

(4) PV devices using ITO only as the hole-extracting electrode exhibit the highest stability, with 30% reduction in efficiency only after ~20 hours testing in air for the champion device, which is very high for an unencapsulated tin perovskite PV device test in air. However, devices using a model semi-transparent 8 nm gold window electrode also exhibit good stability, which indicates that this simplification in device structure could be generalised to other stable hole-extracting electrodes.

(5) The reason for the deterioration in devices using ITO, Au and PEDOT:PSS with time is primarily degradation in J_{sc}. However, analysis of the composition of the upper surface of the $CsSnI_3$ layer recovered from devices tested in ambient air for 24 hours without device encapsulation, reveals that ≤11% of the $CsSnI_3$ film has oxidised to Cs_2SnI_6. Consequently, the deterioration in device efficiency over this time frame does not primarily result from a reduction in the light absorption capability of the perovskite film due to oxidation of the $CsSnI_3$ layer.

(6) Finally, the results of the photoelectron spectroscopy study has shown (for the first time) that when $CsSnI_3$ is synthesised in the presence of $SnCl_2$ as a source of excess Sn the work function of the perovskite is reduced from ~4.85 eV to ~4.45 eV, which is consistent with a reduction in the density of Sn vacancy defects in the perovskite. Notably, this reduction in work function ensures that the work function of $CsSnI_3$ is smaller than most hole-extracting electrode materials used in perovskite and organic PV research, and so in most instances a Schottky contact will be formed that would operate to selectively block the unwanted extraction of electrons. This, combined with the added complexity in fabrication and potential for additional degradation pathways that comes with the inclusion of a HTL into the device architecture, brings into question the rationale for the inclusion of HTL in this type of device.

Conflicts of interest

There are no conflicts to declare.

Acknowledgements

The authors would like to thank the United Kingdom Engineering and Physical Sciences Research Council (EPSRC) for funding (Grant number: EP/L505110/1 & EP/N009096/1), and Philip Bellchambers for preparing a sample for photoelectron spectroscopy. All data supporting this study are provided as supplementary information accompanying this paper.

References

1 A. Kojima, K. Teshima, Y. Shirai and T. Miyasaka, *J. Am. Chem. Soc.*, 2009, **131**, 6050.
2 N. K. Elumalai, M. A. Mahmud, D. Wang and A. Uddin, *Energies*, 2016, **9**, 861.
3 M. Li, H. Gou, I. Al-Ogaidi and N. Wu, *ACS Sustainable Chem. Eng.*, 2013, **1**, 713.
4 G. Flora, D. Gupta and A. Tiwari, *Interdiscip. Toxicol.*, 2012, **5**, 47.
5 F. Giustino and H. J. Snaith, *ACS Energy Lett.*, 2016, **1**, 1233.
6 European Food Safety Authority, *EFSA J.*, 2010, **8**, 1570.
7 W. Huang, J. S. Manser, P. V. Kamat and S. Ptasinska, *Chem. Mater.*, 2016, **28**, 303.
8 A. Babayigit, A. Ethirajan, M. Muller and B. Conings, *Nat. Mater.*, 2016, **15**, 247.
9 I. Chung, J.-H. Song, J. Im, J. Androulakis, C. D. Malliakas, H. Li, A. J. Freeman, J. T. Kenney and M. G. Kanatzidis, *J. Am. Chem. Soc.*, 2012, **134**, 8579.
10 Z. Chen, C. Yu, K. Shum, J. J. Wang, W. Pfenninger, N. Vockic, J. Midgley and J. T. Kenney, *J. Lumin.*, 2012, **132**, 345.
11 J. Zhang, C. Yu, L. Wang, Y. Li, Y. Ren and K. Shum, *Sci. Rep.*, 2014, **4**, 6954.
12 M. H. Kumar, S. Dharani, W. L. Leong, P. P. Boix, R. R. Prabhakar, T. Baikie, C. Shi, H. Ding, R. Ramesh, M. Asta, M. Graetzel, S. G. Mhaisalkar and N. Mathews, *Adv. Mater.*, 2014, **26**, 7122.
13 C. C. Stoumpos, C. D. Malliakas and M. G. Kanatzidis, *Inorg. Chem.*, 2013, **52**, 9019.
14 P. Xu, S. Chen, H.-J. Xiang, X.-G. Gong and S.-H. Wei, *Chem. Mater.*, 2014, **26**, 6068.
15 K. P. Marshall, R. I. Walton and R. A. Hatton, *J. Mater. Chem. A*, 2015, **3**, 11631.
16 T. M. Koh, T. Krishnamoorthy, N. Yantara, C. Shi, W. L. Leong, P. P. Boix, A. C. Grimsdale, S. G. Mhaisalkar and N. Mathews, *J. Mater. Chem. A.*, 2015, **3**, 14996.
17 K. P. Marshall, M. Walker, R. I. Walton and R. A. Hatton, *Nat. Energy*, 2016, **1**, 16178.

 This journal is © The Royal Society of Chemistry 2017

Open Access Article. Published on 06 October 2017. Downloaded on 3/29/2024 1:21:09 PM.
This article is licensed under a Creative Commons Attribution 3.0 Unported Licence.

18 S. Gupta, T. Bendikov, G. Hodes and D. Cahen, *ACS Energy Lett.*, 2016, **1**, 1028.
19 Food Standards Agency, *Current EU approved additives and their E Numbers*, 2016, http://www.food.gov.uk/science/additives/enumberlist.
20 Y. Zhang, X. Hu, L. Chen, Z. Huang, Q. Fu, Y. Liu, L. Zhang and Y. Chen, *Org. Electron.*, 2016, **30**, 281.
21 A. Mei, X. Li, L. Liu, Z. Ku, T. Liu, Y. Rong, M. Xu, M. Hu, J. Chen, Y. Yang, M. Grätzel and H. Han, *Science*, 2014, **345**, 295.
22 L. Meng, J. You, T.-F. Guo and Y. Yang, *Acc. Chem. Res.*, 2016, **49**, 155.
23 W.-Y. Chen, L.-L. Deng, S.-M. Dai, X. Wang, C.-B. Tian, X.-X. Zhan, S.-Y. Xie, R.-B. Huang and L. Zheng, *J. Mater. Chem. A*, 2015, **3**, 19353.
24 W. Sun, S. Ye, H. Rao, Y. Li, Z. Liu, L. Xiao, Z. Chen, Z. Bian and C. Huang, *Nanoscale*, 2016, **8**, 15954.
25 J. A. Christians, R. C. M. Fung and P. V. Kamat, *J. Am. Chem. Soc.*, 2014, **136**, 758.
26 H.-B. Kim, H. Choi, J. Jeong, S. Kim, B. Walker, S. Song and J. Y. Kim, *Nanoscale*, 2014, **6**, 6679.
27 X. Bao, Y. Wang, Q. Zhu, N. Wang, D. Zhu, J. Wang, A. Yang and R. Yang, *J. Power Sources*, 2015, **297**, 53.
28 J.-Y. Jeng, Y.-F. Chiang, M.-H. Lee, S.-R. Peng, T.-F. Guo, P. Chen and T.-C. Wen, *Adv. Mater.*, 2013, **25**, 3727.
29 H. M. Stec, R. J. Williams, T. S. Jones and R. A. Hatton, *Adv. Funct. Mater.*, 2011, **21**, 1709.
30 H. M. Stec and R. A. Hatton, *ACS Appl. Mater. Interfaces*, 2012, **4**, 6013.
31 D. Moghe, L. Wang, C. J. Traverse, A. Redoute, M. Sponseller, P. R. Brown, V. Bulović and R. R. Lunt, *Nano Energy*, 2016, **28**, 469.
32 W. Liao, D. Zhao, Y. Yu, C. R. Grice, C. Wang, A. J. Cimaroli, P. Schulz, W. Meng, K. Zhu, R. G. Xiong and Y. Yan, *Adv. Mater.*, 2016, **28**, 9333.
33 F. Hao, C. C. Stoumpos, D. H. Cao, R. P. H. Chang and M. G. Kanatzidis, *Nat. Photonics*, 2014, **8**, 489.
34 Thin Film Center Inc., 2013.
35 C. F. Macrae, I. J. Bruno, J. A. Chisholm, P. R. Edgington, P. McCabe, E. Pidcock, L. Rodriguez-Monge, R. Taylor, J. Van De Streek and P. A. Wood, *J. Appl. Crystallogr.*, 2008, **41**, 466.
36 N. Fairley, *CasaXPS*, Casa Software Ltd., 2016.
37 I. Horcas, R. Fernández, J. M. Gómez-Rodríguez, J. Colchero, J. Gómez-Herrero and A. M. Baro, *Rev. Sci. Instrum.*, 2007, **78**, 13705.
38 C. A. Schneider, W. S. Rasband and K. W. Eliceiri, *Nat. Methods*, 2012, **9**, 671.
39 J. Zhou, D. H. Anjum, L. Chen, X. Xu, I. A. Ventura, L. Jiang and G. Lubineau, *J. Mater. Chem. C*, 2014, **2**, 9903.
40 A. M. A. Leguy, Y. Hu, M. Campoy-Quiles, M. I. Alonso, O. J. Weber, P. Azarhoosh, M. van Schilfgaarde, M. T. Weller, T. Bein, J. Nelson, P. Docampo and P. R. F. Barnes, *Chem. Mater.*, 2015, **27**, 3397.
41 G. B. Kauffman, L. Y. Fang, N. Viswanathan and G. Townsend, *Inorg. Synth.*, 2006, **22**, 101.
42 F. Hao, C. C. Stoumpos, P. Guo, N. Zhou, T. J. Marks, R. P. H. Chang and M. G. Kanatzidis, *J. Am. Chem. Soc.*, 2015, **137**, 11445.
43 T. A. Berhe, W.-N. Su, C.-H. Chen, C.-J. Pan, J.-H. Cheng, H.-M. Chen, M.-C. Tsai, L.-Y. Chen, A. A. Dubale and B.-J. Hwang, *Energy Environ. Sci.*, 2016, **9**, 323.
44 N. K. Noel, S. D. Stranks, A. Abate, C. Wehrenfennig, S. Guarnera, A.-A. Haghighirad, A. Sadhanala, G. E. Eperon, S. K. Pathak, M. B. Johnston, A. Petrozza, L. M. Herz and H. J. Snaith, *Energy Environ. Sci.*, 2014, **7**, 3061.
45 Q. Bao, X. Liu, S. Braun and M. Fahlman, *Adv. Energy Mater.*, 2014, **4**, 1301272.
46 Q. D. Yang, T.-W. Ng, M.-F. Lo, F. Y. Wang, N. B. Wong and C.-S. Lee, *J. Phys. Chem. C*, 2012, **116**, 10982.
47 P. Peumans, A. Yakimov and S. R. Forrest, *J. Appl. Phys.*, 2003, **93**, 3693.
48 Z. R. Hong, Z. H. Huang and X. T. Zeng, *Thin Solid Films*, 2007, **515**, 3019.
49 A. Guerrero, P. P. Boix, L. F. Marchesi, T. Ripolles-Sanchis, E. C. Pereira and G. Garcia-Belmonte, *Sol. Energy Mater. Sol. Cells*, 2012, **100**, 185.
50 T. S. Glen, N. W. Scarratt, H. Yi, A. Iraqi, T. Wang, J. Kingsley, A. R. Buckley, D. G. Lidzey and A. M. Donald, *Sol. Energy Mater. Sol. Cells*, 2015, **140**, 25.
51 C. M. Proctor, J. A. Love and T. Q. Nguyen, *Adv. Mater.*, 2014, **26**, 5957.
52 B. Lee, C. C. Stoumpos, N. Zhou, F. Hao, C. Malliakas, C. Yeh, T. J. Marks, M. G. Kanatzidis and R. P. H. Chang, *J. Am. Chem. Soc.*, 2014, **136**, 15379.
53 B. Saparov, J.-P. Sun, W. Meng, Z. Xiao, H.-S. Duan, O. Gunawan, D. Shin, I. G. Hill, Y. Yan and D. B. Mitzi, *Chem. Mater.*, 2016, **28**, 2315.
54 H. Yoshida, *Anal. Bioanal. Chem.*, 2014, **406**, 2231.
55 T. S. Glen, N. W. Scarratt, H. Yi, A. Iraqi, T. Wang, J. Kingsley, A. R. Buckley, D. G. Lidzey and A. M. Donald, *J. Polym. Sci., Part B: Polym. Phys.*, 2016, **54**, 216.
56 M.-C. Jung, S. R. Raga, L. K. Ono and Y. Qi, *Sci. Rep.*, 2015, **5**, 9863.
57 W. Nie, H. Tsai, R. Asadpour, A. J. Neukirch, G. Gupta, J. J. Crochet, M. Chhowalla, S. Tretiak, M. A. Alam and H. Wang, *Science*, 2015, **347**, 522.
58 M. P. de Jong, L. J. van Ijzendoorn and M. J. A. de Voigt, *Appl. Phys. Lett.*, 2000, **77**, 2255.
59 S. Aharon, S. Gamliel, B. El Cohen and L. Etgar, *Phys. Chem. Chem. Phys.*, 2014, **16**, 10512.